NASA-CR-194173

IN-32-CR

INTERIM Report No: TRC-EM-CAB-9306

OCIT

ANALYTIC

(1+2)

HIGH-FREQUENCY TECHNIQUES FOR RCS PREDICTION OF PLATE GEOMETRIES
AND
A PHYSICAL OPTICS/EQUIVALENT CURRENTS MODEL FOR THE RCS OF TRIHEDRAL CORNER REFLECTORS

Semiannual Progress Report

PART I

Constantine A. Balanis and Lesley A. Polka

February 1, 1993 - July 31, 1993

PART II

Constantine A. Balanis and Anastasis C. Polycarpou

February 1, 1993 - July 31, 1993

Telecommunications Research Center
College of Engineering and Applied Science
Arizona State University
Tempe,   AZ 85287-7206

N94-20269
—THRU—
N94-20271
Unclas

G3/32   0185950

(NASA-CR-194173) [RCS ANALYSIS OF PLATE GEOMETRIES, PARTS 1 AND 2] Semiannual Progress Report, 1 Feb. - 31 Jul. 1993 (Arizona State Univ.) 43 p

HIGH-FREQUENCY TECHNIQUES FOR RCS PREDICTION OF PLATE GEOMETRIES
AND
A PHYSICAL OPTICS/EQUIVALENT CURRENTS MODEL FOR THE RCS OF TRIHEDRAL CORNER REFLECTORS

Semiannual Progress Report

PART I

Constantine A. Balanis and Lesley A. Polka

February 1, 1993 - July 31, 1993

PART II

Constantine A. Balanis and Anastasis C. Polycarpou

February 1, 1993 - July 31, 1993

Telecommunications Research Center
College of Engineering and Applied Science
Arizona State University
Tempe, AZ 85287-7206

Abstract

Part I of this report presents a Uniform Theory of Diffraction (UTD) model for the principal-plane radar cross section (RCS) of a perfectly conducting, rectangular plate coated on one side with an electrically thin ($t \ll \lambda$), lossy dielectric. The incorporation of higher-order, multiple diffractions and of multiply diffracted surface-waves is discussed in detail. It is demonstrated that these terms are crucial to obtaining an accurate model. Approximations that are used in the model are discussed. Suggestions for improvements to the model are made. Validation is provided via comparison with experimental data and a physical optics (PO) model.

Part II of this report examines the scattering in the interior regions of both square and triangular trihedral corner reflectors. The theoretical model presented combines geometrical and physical optics (GO and PO), used to account for reflection terms, with equivalent edge currents (EEC), used to account for first-order diffractions from the edges. First-order, second-order, and third-order reflection terms are included. Calculating the first-order reflection terms involves integrating over the entire surface of the illuminated plate. Calculating the second- and third-order reflection terms, however, is much more difficult because the illuminated area is an arbitrary polygon whose shape is dependent upon the incident angles. The method for determining the area of integration is detailed in this report. Extensive comparisons between the high-frequency model, Finite-Difference Time-Domain (FDTD) and experimental data are used for validation of the RCS of both square and triangular trihedral reflectors.

I. HIGH-FREQUENCY TECHNIQUES FOR RCS PREDICTION OF PLATE GEOMETRIES

A. INTRODUCTION

Important research areas involving high-frequency scattering prediction techniques that have been discussed in previous reports include the development of techniques for modeling corner diffraction, nonprincipal-plane scattering, and scattering from coated conducting geometries [1, 2, 3, 4, 5, 6, 7, 8, 9]. The most recent reports have dealt mainly with the principal-plane radar cross section (RCS) prediction of a perfectly conducting rectangular plate coated on one side with an electrically thin $(t \ll \lambda)$, lossy dielectric [3, 4, 5, 6, 7, 8, 9]. This is an important geometry to consider because its simplicity allows the isolation of individual scattering mechanisms while its generality enables its incorporation into more complex modeling geometries. In other words, the plate geometry allows one to develop and validate modeling techniques for higher-order mechanisms, such as multiple diffractions and multiply diffracted surface waves, with the eventual goal of being able to apply these techniques to general, coated conducting geometries.

This report presents and validates a Uniform Theory of Diffraction (UTD) model for the principal-plane RCS prediction of a coated conducting rectangular plate. The incorporation of higher-order multiple diffraction terms and of higher-order surface-wave terms is discussed. The necessity of including higher-order mechanisms is demonstrated. The model is validated by comparisons with experimental results, and its superiority over a simple physical optics (PO) model is demonstrated. Other models exist for the coated plate geometry [10, 11]; however, the model presented in this report incorporates higher-order terms which were not included in these earlier models. Specifically, the work by Knop and Cohn [10] is based upon a physical optics (PO) approach, which does not include edge ef-

fects. The model presented by Bhattacharyya and Tadon [11], although similar in approach to the method used in this report, includes only first- and second-order diffractions. The model presented here includes first-, second-, and third-order regular diffractions and second- and third-order surface-wave diffractions. These additional terms are crucial to obtaining accurate results.

The modeling of the scattered fields from coated conducting targets is a subject of interest both to those developing low-frequency modeling techniques and to those developing high-frequency techniques. The development of low-frequency techniques has been quite successful. Both the moment method (MM) and the finite-difference time-domain (FDTD) techniques can be used to accurately predict the RCS of a coated plate [12]. Because these techniques are low-frequency techniques, the size of the geometry that can easily be modeled is limited by computational time and memory requirements. Thus, it is important to develop high-frequency techniques, which are inherently more appropriate for electrically large structures.

The model developed in this report is based upon the UTD diffraction coefficients for an impedance wedge [13, 14]. The effects of the finite thickness lossy coating backed by a perfect conductor are included using the short-circuited transmission-line approximation. Although a simple model, it will be demonstrated that this model is accurate near and at normal incidence and sufficient for other angles. The model presented in this report is computationally fast and simple and increases in accuracy as the electrical size of the geometry increases and as the electrical thickness of the coating becomes smaller. These are desirable and expected properties of a high-frequency method.

Other work on high-frequency methods for modeling coated conducting geometries includes more sophisticated ways of dealing with problems of importance. For example, Herman and Volakis [15] have dealt extensively with the modeling of scatterers in overlapping transition regions using the Extended Spectral Ray Method (ESRM). Volakis and Senior [16] have investigated the scattering

3

by a metal-backed dielectric half plane using higher-order generalized impedance boundary conditions. Rojas and Chou [17] have also explored solutions to partially coated conducting geometries using generalized impedance boundary conditions. Finally, Bernard [18] developed a solution for the specific case of a conducting wedge covered by a dielectric material. Because all of this work focuses on specific problems inherent in developing high-frequency techniques for dealing with coated conductors, the results obtained are highly accurate for the problems of interest. The techniques are not inherently easy to apply to more general geometries. The goal of the research outlined in this report is to develop general models, for coated conducting geometries, that are easily implemented and computationally fast and accurate. Thus, the model outlined in this report uses a simple boundary condition, the impedance boundary condition, which is incorporated into the short-circuited transmission-line approximation, to model the effects of a finite-thickness coating backed by a perfect conductor. Also, a straightforward application of the UTD, based upon the coefficients for the impedance wedge, is applied. Future research will attempt to incorporate ideas from the aforementioned research into the general model.

B. THEORY AND RESULTS

1. UTD Plate Model

The UTD plate model consists of two parallel impedance wedges separated by a distance, w, equal to the plate width. The wedge geometry is shown in Fig. 1. To obtain the plate model illustrated in Fig. 2, the left and right wedge included angles are set to $0°$, or the wedge parameter is set to $n = 2$. For the coated plate, the bottom face of each wedge is modeled as a perfect conductor with $\eta_2 = 0$. The top face of each wedge is modeled by an equivalent impedance appropriate for the coating. The plate is modeled two-dimensionally in the principal plane, and
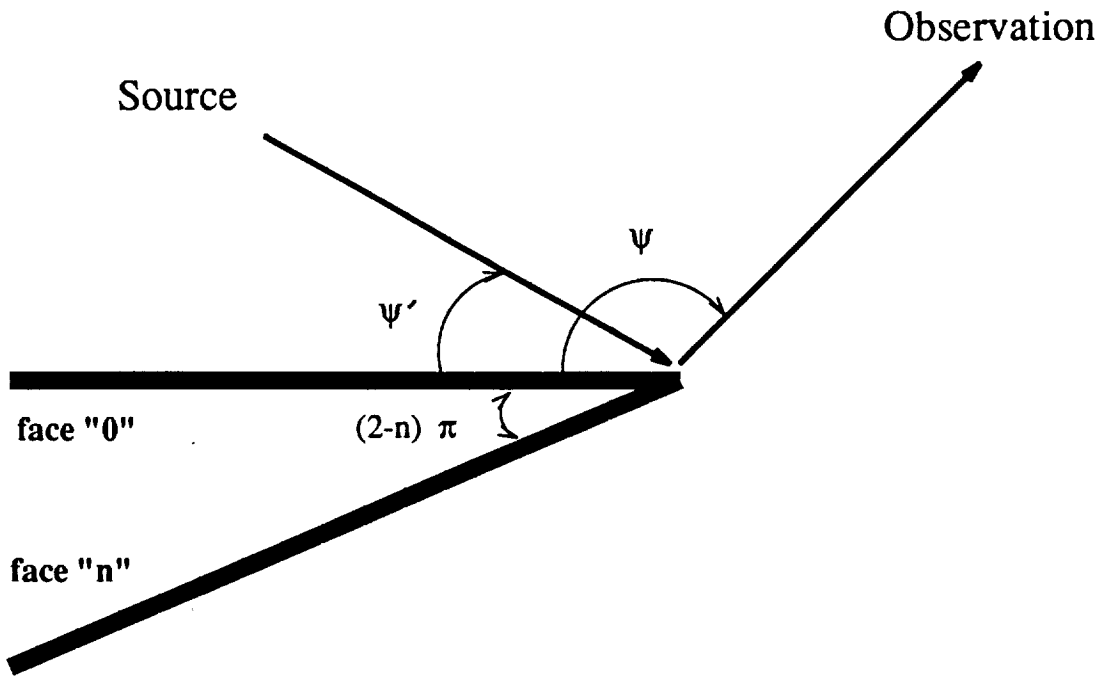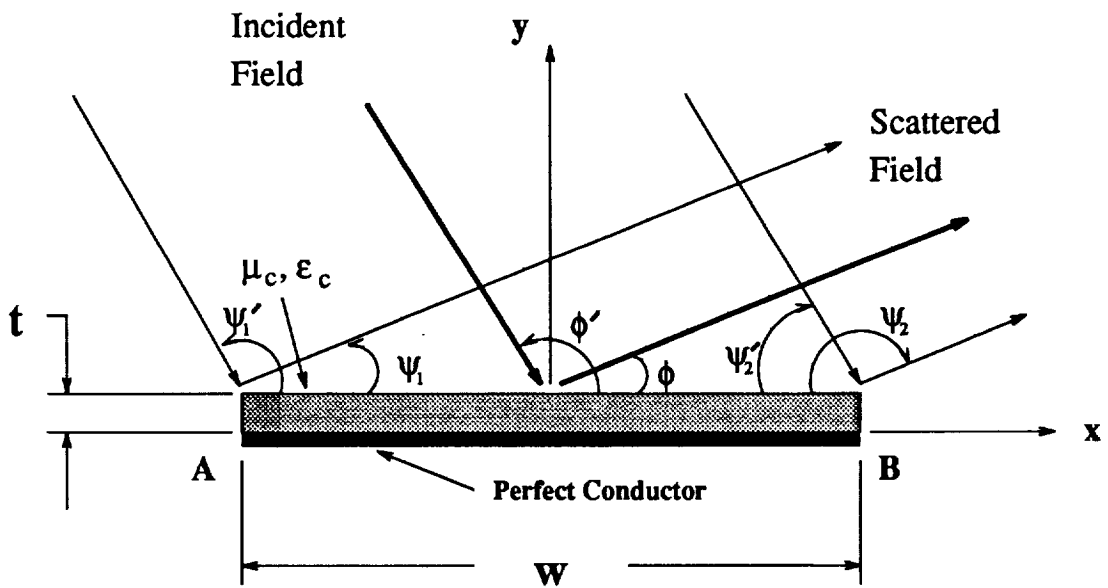
4

Figure 1: Impedance wedge geometry.

Figure 2: Geometry for principal-plane scattering from a strip/plate with a finite-thickness coating backed by a perfect conductor.

three-dimensional results are obtained using Ross's truncation approximation [19]:

$$\sigma_{3-D} = \frac{2L^2}{\lambda}\sigma_{2-D} \qquad (1)$$

It is important that the impedance of the coating be modeled accurately, yet simply, so that the model remains computationally fast and easy to implement. For these reasons, the short-circuited transmission-line approximation is used to express the normalized equivalent impedance of the top face of each wedge as [8]:

$$\eta_0 = j\sqrt{\frac{\mu_c}{\epsilon_c}}\tan\left(2\pi\sqrt{\mu_c\epsilon_c}t\right) \qquad (2)$$

where μ_c and ϵ_c are the relative permeability and permittivity, respectively, of the coating; and t is the thickness of the coating in free-space wavelengths. Both μ_c and ϵ_c can be complex numbers, so η_0 is usually a complex quantity.

A first-order model which accounts for diffractions from each of the wedges comprising the plate is not sufficient for accurate RCS prediction. As will be demonstrated, interactions between the wedges are crucial scattering mechanisms. The model of this work contains second- and third-order diffraction terms, in addition to first-order mechanisms. Also, second- and third-order surface-wave terms are included.

Higher-order diffraction terms are formulated by consecutively multiplying the appropriate diffraction coefficients by the phase and amplitude spreading factors. The diffraction coefficients used are the UTD coefficients derived by Tiberio, et al. [13], and further revised by Griesser and Balanis [14]. These were based upon Maliuzhinets' solution for the scattering by an impedance wedge [20]. The particular coefficients and methods of calculation were explicitly detailed in a previous report [8] and, therefore, will not be repeated here. For reference, the notation for the specific coefficients, their particular use, and the number of the equation in [8] that gives the expression for the coefficient are given in the following table:

6

Table of Coefficients		
Usage	Notation	Equation Reference in [8]
1st-order Diffractions (Plane-wave Incidence, Far-field Observation)	$D_{ff}(\psi', \psi, \theta_0, \theta_2 = 0, n = 2)$	Eq. (4) with Fresnel Functions set to unity ($F[x] = 1$)
Higher-order Diffractions (Plane-wave Incidence, Observation at a Finite Distance)	$D_{pwfd}(\rho', \psi', \psi, \theta_0, \theta_2 = 0, n = 2)$	Eq. (4)
Higher-order Diffractions (Cylindrical-wave Incidence, Far-field Observation)	$D_{cwff}(\rho, \psi', \psi, \theta_0, \theta_2 = 0, n = 2)$	Eq. (4) with ρ substituted for ρ' and ψ' and ψ switched
Surface Wave Field	$U_{sw}(\rho, \psi', \psi, \theta_0, n = 2)$	Eq. (19)
Surface Wave Transition Field	$U_{swtr}(\rho, \psi', \psi, \theta_0, n = 2)$	Eq. (21)

The angles of incidence and observation with respect to the wedge of interest are ψ' and ψ, respectively. In [8], these were designated as ϕ' and ϕ. The distance from the source to the point of diffraction is ρ' while ρ is the diffraction distance. The Brewster angles, θ_0 and θ_n, of the top and bottom faces of the wedge are, respectively, given by Eqs. (2) and (3) of [8]. The wedge parameter is n, and it is equal to 2 for a half plane.

The second-order diffracted fields actually consist of four mechanisms; two emanating from each edge of the plate. Fig. 3 illustrates the mechanisms for the right side of the plate. The field incident on the left side of the plate diffracts along both the top and bottom of the plate. Each of these diffracted fields then diffracts from the right side of the plate. Analogous mechanisms exist for the left side of the plate for a total of four second-order mechanisms. The total second-order diffracted field is:

$$E_{2nd} = E_1 \frac{e^{-jk\rho}}{\sqrt{k\rho}} \frac{e^{-jkw}\sqrt{k}}{2\sqrt{w}} \left\{ e^{j\frac{kw}{2}(\cos\phi' - \cos\phi)} \right.$$

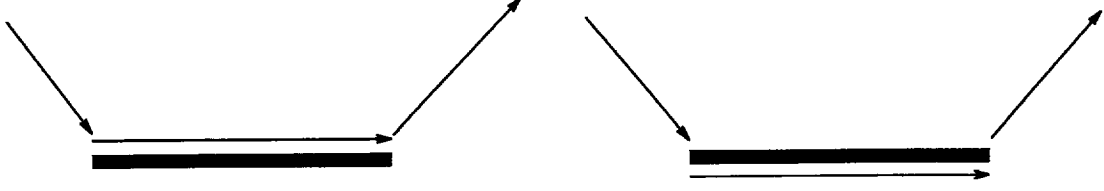Figure 3: Second-order scattering terms emanating from the right edge of the plate.

$$\times \quad [D_{pwfd}(w, \psi_2', 0°, \theta_0, \theta_2 = 0, n = 2)$$

$$\times \quad D_{cwff}(w, 0°, \psi_1, \theta_0, \theta_2 = 0, n = 2)$$

$$+ \quad D_{pwfd}(w, \psi_2', 360°, \theta_0, \theta_2 = 0, n = 2)$$

$$\times \quad D_{cwff}(w, 360°, \psi_1, \theta_0, \theta_2 = 0, n = 2)]$$

$$+ \quad e^{-j\frac{kw}{2}(\cos\phi' - \cos\phi)}$$

$$\times \quad [D_{pwfd}(w, \psi_1', 0°, \theta_0, \theta_2 = 0, n = 2)$$

$$\times \quad D_{cwff}(w, 0°, \psi_2, \theta_0, \theta_2 = 0, n = 2)$$

$$+ \quad D_{pwfd}(w, \psi_1', 360°, \theta_0, \theta_2 = 0, n = 2)$$

$$\times \quad D_{cwff}(w, 360°, \psi_2, \theta_0, \theta_2 = 0, n = 2)]\} \qquad (3)$$

The third-order diffracted field consists of eight scattering mechanisms. The four emanating from the right side of the plate are demonstrated in Fig. 4. Four analogous mechanisms exist for the left side of the plate. The total third-order diffracted field is:

$$\mathbf{E_{3rd}} = \mathbf{E_i} \frac{e^{-jk\rho}}{\sqrt{k\rho}} \frac{e^{-j2kw}\sqrt{k}}{4w} \{ e^{-j\frac{kw}{2}(\cos\phi' + \cos\phi)}$$

$$\times \quad [D_{pwfd}(w, \psi_1', 0°, \theta_0, \theta_2 = 0, n = 2)$$
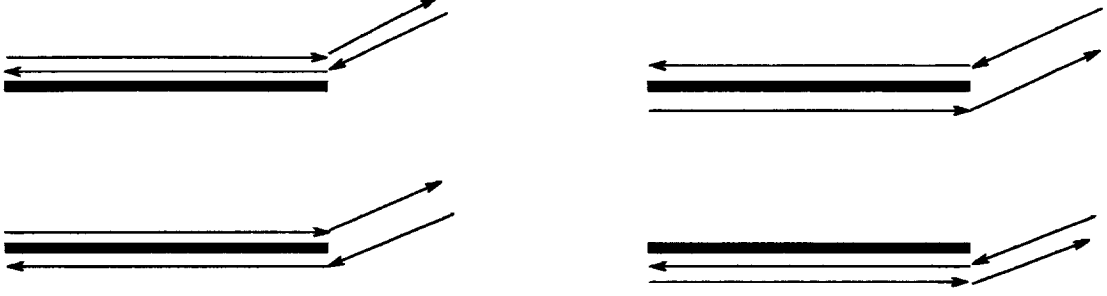
$$\times \quad D_{cwff}(w, 0°, \psi_1, \theta_0, \theta_2 = 0, n = 2)$$

8

Figure 4: Third-order scattering terms emanating from the right edge of the plate.

$$\times \quad D_{cwff}(\frac{w}{2}, 0°, 0°, \theta_0, \theta_2, n = 2)$$

$$+ \quad D_{pwfd}(w, \psi_1', 360°, \theta_0, \theta_2 = 0, n = 2)$$

$$\times \quad D_{cwff}(w, 360°, \psi_1, \theta_0, \theta_2 = 0, n = 2)$$

$$\times \quad D_{cwff}(\frac{w}{2}, 360°, 360°, \theta_0, \theta_2, n = 2)$$

$$+ \quad D_{pwfd}(w, \psi_1', 0°, \theta_0, \theta_2 = 0, n = 2)$$

$$\times \quad D_{cwff}(w, 360°, \psi_1, \theta_0, \theta_2 = 0, n = 2)$$

$$\times \quad D_{cwff}(\frac{w}{2}, 0°, 360°, \theta_0, \theta_2, n = 2)$$

$$+ \quad D_{pwfd}(w, \psi_1', 360°, \theta_0, \theta_2 = 0, n = 2)$$

$$\times \quad D_{cwff}(w, 0°, \psi_1, \theta_0, \theta_2 = 0, n = 2)$$

$$\times \quad D_{cwff}(\frac{w}{2}, 360°, 0°, \theta_0, \theta_2, n = 2)\Big]$$

$$+ \quad e^{j\frac{kw}{2}(\cos\phi' + \cos\phi)}$$

$$\times \quad [D_{pwfd}(w, \psi_2', 0°, \theta_0, \theta_2 = 0, n = 2)$$

$$\times \quad D_{cwff}(w, 0°, \psi_2, \theta_0, \theta_2 = 0, n = 2)$$

$$\times \quad D_{cwff}(\frac{w}{2}, 0°, 0°, \theta_0, \theta_2, n = 2)$$

9

$$+ \quad D_{pwfd}(w, \psi_2', 360°, \theta_0, \theta_2 = 0, n = 2)$$

$$\times \quad D_{cwff}(w, 360°, \psi_2, \theta_0, \theta_2 = 0, n = 2)$$

$$\times \quad D_{cwff}(\frac{w}{2}, 360°, 360°, \theta_0, \theta_2, n = 2)$$

$$+ \quad D_{pwfd}(w, \psi_2', 0°, \theta_0, \theta_2 = 0, n = 2)$$

$$\times \quad D_{cwff}(w, 360°, \psi_2, \theta_0, \theta_2 = 0, n = 2)$$

$$\times \quad D_{cwff}(\frac{w}{2}, 0°, 360°, \theta_0, \theta_2, n = 2)$$

$$+ \quad D_{pwfd}(w, \psi_2', 360°, \theta_0, \theta_2 = 0, n = 2)$$

$$\times \quad D_{cwff}(w, 0°, \psi_2, \theta_0, \theta_2 = 0, n = 2)$$

$$\times \quad D_{cwff}(\frac{w}{2}, 360°, 0°, \theta_0, \theta_2, n = 2) \Big] \Big\} \qquad (4)$$

In the above equation, $\frac{w}{2}$ is used at some points as the distance parameter because the diffraction coefficient at these points is for cylindrical-wave incidence from a distance of w and observation at a finite distance of w. For this case, a distance parameter of $\frac{\rho'\rho}{\rho'+\rho} = \frac{w}{2}$ must be used. Another point of greater importance is that the UTD diffraction coefficients for the impedance wedge developed in [13] are identically zero for grazing incidence, which is the angle of incidence necessary for incorporating higher-order diffraction terms. Tiberio, et al., performed a more precise expansion of Maluizhinets' solution to the impedance wedge problem and, thus, developed an appropriate diffraction coefficient for the case of grazing incidence (see [13] Eq. (16)). The incorporation of this coefficient into our model is a future goal of this research. For the results generated in this report, the value of the diffraction coefficient for grazing incidence is calculated $\frac{1}{100}th$ of a degree from grazing using the ordinary UTD coefficients of Eq. (4) in [8]. The results using this approximation are quite good, as will be demonstrated in the results section of this report. It is expected that incorporating the more precise coefficient of Eq. (16) in [13] will achieve even better results.

Surface wave fields exist only for certain angular regions and surface impedances given by Eqs. (17) and (18) in [8]. Surface wave transition fields compensate for discontinuities in the surface wave field at the surface wave shadow boundaries in a manner analogous to the way in which diffracted fields compensate for discontinuities in the geometrical optics field at the incident and reflection shadow boundaries. The surface wave transition fields also add to the total field everywhere, as do the diffracted fields.

The model of this report includes second- and third-order diffracted surface wave and surface-wave transition fields. The expressions for the total fields are cumbersome and similar in form to Eqs. (3) and (4) above, so they will not be included here. The general expression for the total nth-order diffracted field, including the surface wave and surface wave transition terms is:

$$
\begin{aligned}
\mathbf{U}_{nth} &= \mathbf{U}_i \prod_{i=1}^{n-1} \left[D(\psi_i', \psi_i, \rho_i) \frac{e^{-jk\rho_i}}{\sqrt{\rho_i}} + U_{sw_i} + U_{swtr_i} \right] \\
&\times \quad D(\psi_n', \psi_n, \rho_n) \frac{e^{-jk\rho}}{\sqrt{\rho}}
\end{aligned}
\tag{5}
$$

2.   Contributions of Higher-Order Scattering Mechanisms

Although a model that includes first-order diffractions is accurate near and at normal incidence to the plate, it is an insufficient model for accurately predicting the scattering at all angles. For angles away from normal incidence, higher-order diffraction terms and surface wave terms are crucial. A breakdown of the contributions of the various terms is shown in Figs. 5 - 8 for a 2λ by 2λ plate coated on one side with a coating of thickness $t = 0.04121\lambda$ and with material parameters $\mu_c = 1.539 - j1.2241$ and $\epsilon_c = 11.826 - j0.16639$. The results are shown for a frequency of 10 GHz. In all the figures, the solid black line represents the total field calculated using the UTD model. This model includes first-, second-, and third-order regular diffractions, and second- and third-order surface wave and surface wave transition terms.
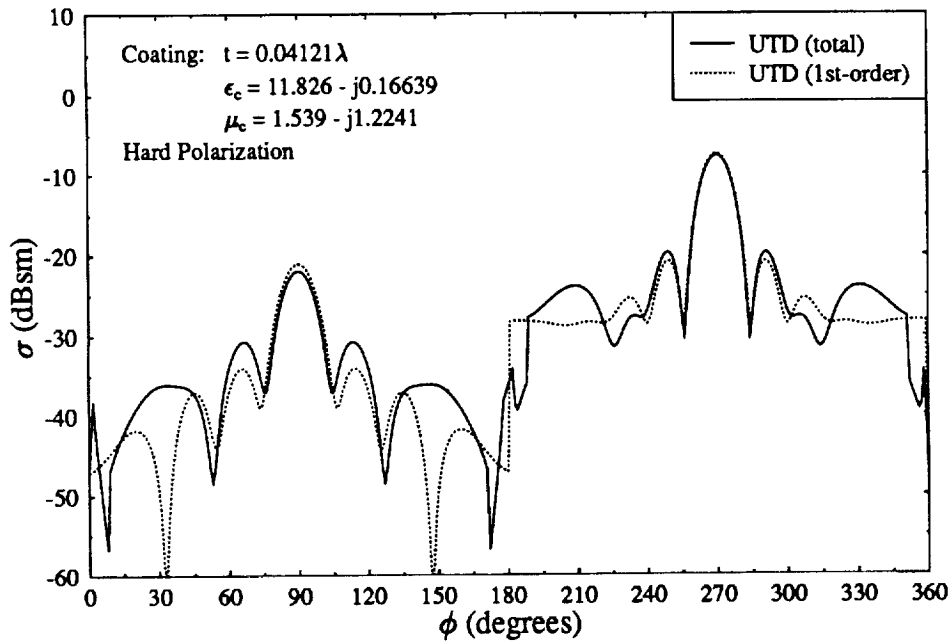
11

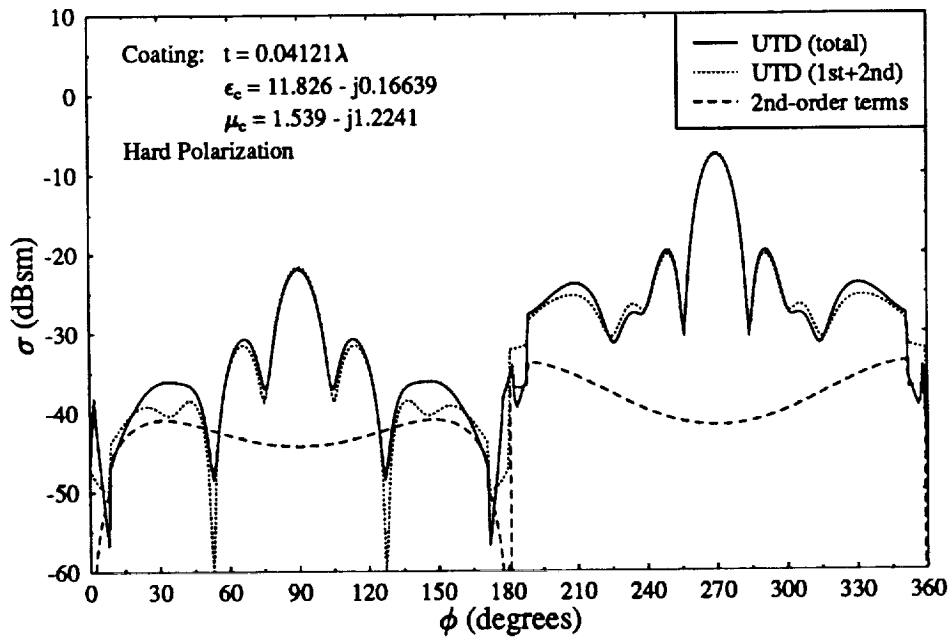Figure 5: Breakdown of the UTD components ($w = L = 2.0\lambda$, $f = 10.0$ GHz).

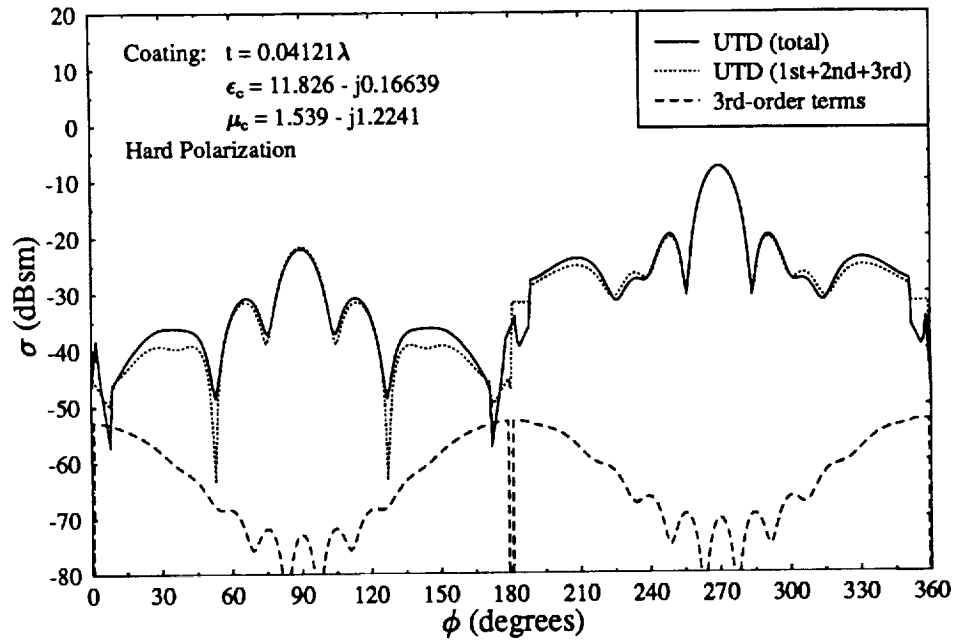Figure 6: Breakdown of the UTD components ($w = L = 2.0\lambda$, $f = 10.0$ GHz).

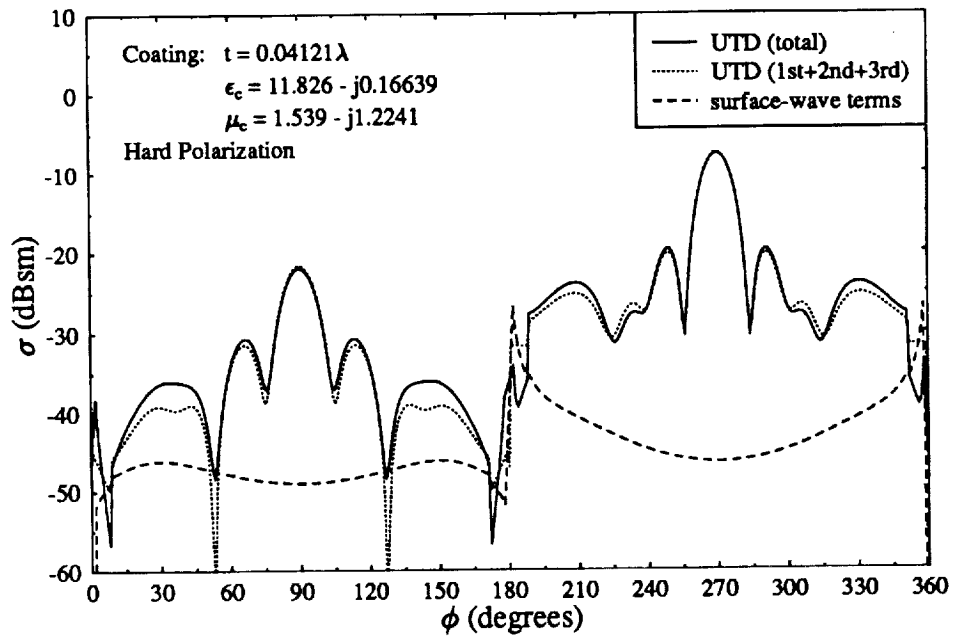Figure 7: Breakdown of the UTD components ($w = L = 2.0\lambda$, $f = 10.0$ GHz).

Figure 8: Breakdown of the UTD components ($w = L = 2.0\lambda$, $f = 10.0$ GHz).

Fig. 5 compares the total UTD field to the field calculated using only first-order diffractions. Near and at normal incidence to both sides of the plate, the two models agree fairly well indicating that first-order diffractions are the main contributing mechanisms at these angles. Away from the main lobe, however, it is apparent that higher-order terms are major contributors to the scattered field. The two models differ drastically in the region extending from grazing incidence to approximately 60° away from grazing on both sides of the plate.

Fig. 6 illustrates that second-order diffractions are the major higher-order contributing mechanisms. The dotted line in this figure is the UTD field calculated using only first- and second-order diffraction terms. The dashed line is the magnitude of the second-order diffractions only. For the main lobe on both sides of the plate, the second-order terms are not significant; however, away from this lobe, they become crucial. The first minor lobes are predicted fairly well with the addition of the second-order terms. In the grazing lobes, especially on the coated side of the plate, there is still a need for higher-order terms to complete the model.

The third-order diffraction terms improve the results in the grazing lobes somewhat, as illustrated in Fig. 7, where the dotted line represents a UTD model containing first-, second-, and third-order regular diffractions. The dashed line representing the magnitude of the third-order field indicates that these fields are very minor compared to the other fields. Fig. 8 illustrates that surface wave and surface wave transition fields are crucial to the overall RCS pattern in the grazing lobes. The solid line is the total field containing the surface wave and surface wave transition fields while the dotted line does not contain these terms. The difference between the two predicted fields is obvious in the lobes near grazing. As the dashed line representing the magnitude of the surface wave and surface wave transition fields indicates, the surface wave fields represent a larger contribution to the total field than the third-order fields.

3. Results

To validate the coated plate UTD model, measured RCS data was obtained for two different physical plates at several different frequencies using the ElectroMagnetic Anechoic Chamber (EMAC) at Arizona State University (ASU). The two plates, which will be referred to as Plate A and Plate B, are characterized by the following parameters:

- Plate A
    - size: 6.0 cm × 6.0 cm
    - plate material: Aluminum (25.0 mils)
    - coating material: SWAM (commercially available ferrite-loaded RAM)
    - coating thickness: 48.642 mils
    - relative permittivity of coating: $\epsilon_c = 11.826 - j0.16639$
    - relative permeability of coating: $\mu_c = 1.539 - j1.2241$
    - frequency of measurement: 10.0 GHz
    - plate size in wavelengths: $2.0\lambda \times 2.0\lambda$
    - coating thickness in wavelengths: 0.04121λ

- Plate B
    - size: 3.1625 in. × 3.1625 in.
    - plate material: Brass (10.0 - 15.0 mils)
    - coating material: GDS (commercially available ferrite-loaded RAM)
    - coating thickness: 33.177 mils
    - relative permittivity of coating: $\epsilon_c = 13.927 - j0.208$
    - relative permeability of coating: $\mu_c = 1.446 - j1.140$
    - frequencies of measurement: 9.4842 GHz, 11.1964 GHz, and 12.053 GHz
    - plate sizes in wavelengths: $2.54\lambda \times 2.54\lambda$, $3.0\lambda \times 3.0\lambda$, and $3.23\lambda \times 3.23\lambda$
    - coating thicknesses in wavelengths: 0.0267λ, 0.03147λ, 0.03388λ

Plate A is electrically smaller than Plate B, and Plate A has a lossier coating than Plate B. For these reasons, the UTD model is less accurate for Plate A than it is for Plate B. The data indicates that the UTD model improves in accuracy as the electrical size of the plate increases and as the coating becomes electrically thinner
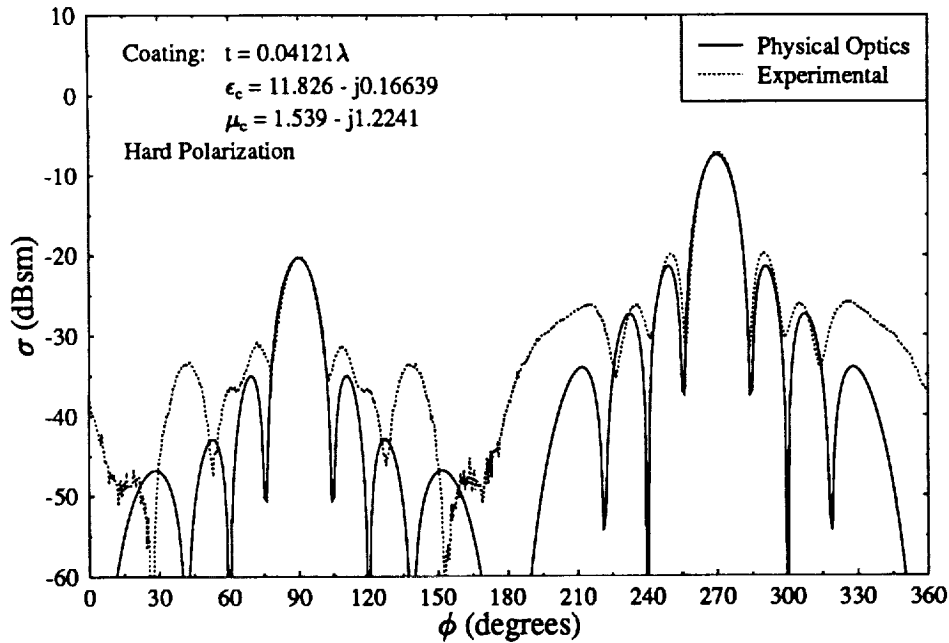
15

Figure 9: Monostatic RCS of Plate A ($w = L = 2.0\lambda$, $f = 10.0$ GHz).

and less lossy. The data presented in the next few figures demonstrates that the UTD model, which accounts for edge effects, is much more accurate than the PO model, which does not include the effects of interacting edges.

Fig. 9 contains graphs of the PO and experimental data for Plate A. Although there is excellent agreement in the main lobe, the PO model becomes increasingly inaccurate away from the main lobe, especially on the coated side of the plate ($0° < \phi < 180°$). Fig. 10 demonstrates that the UTD model is much more accurate. On the perfectly conducting side of the plate, the UTD model agrees fairly well in the main lobe and first two side lobes. On the coated side of the plate, there is much inaccuracy; however, the results are still better than those obtained using the PO model. The two biggest areas of concern are the discontinuities apparent at the grazing angles near $\phi = 180°$ and the discrepancy at normal incidence to the coated side of the plate. These areas are being investigated.
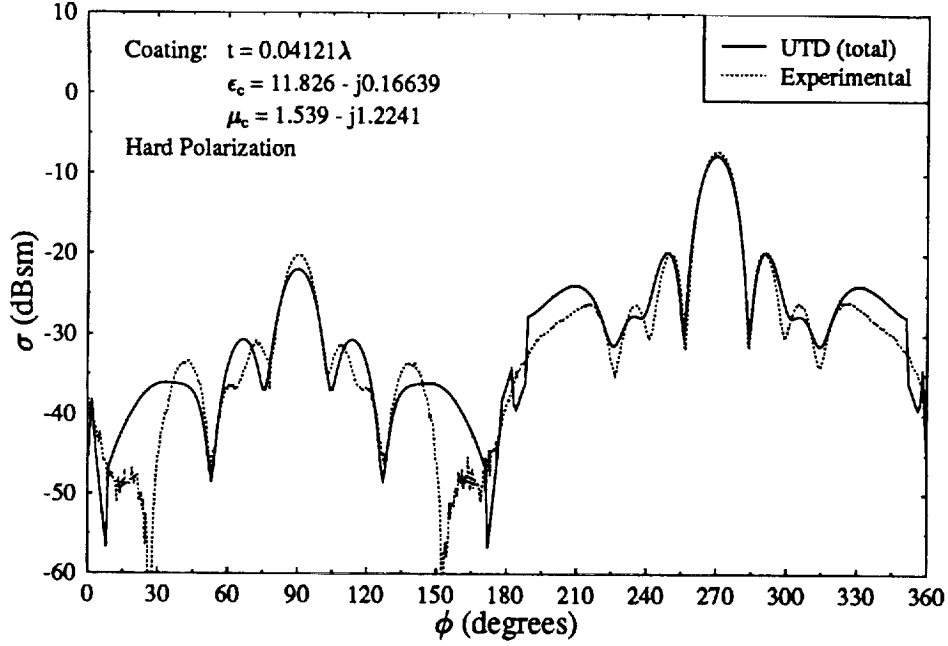
16

Figure 10: Monostatic RCS of Plate A ($w = L = 2.0\lambda$, $f = 10.0$ GHz).

The results for Plate B demonstrate that the UTD model becomes much more accurate as the electrical size of the plate increases. Fig. 11 contains PO and experimental data for Plate B at 9.5 GHz. Agreement between the two sets of data is excellent for the main lobe and first side lobe on both sides of the plate; however, the agreement between the UTD data and the experimental results, shown in Fig. 12, shows much better agreement. On both sides of the plate, agreement is almost exact in the main lobe and first two side lobes. Agreement even in the grazing lobes is very good. At higher operational frequencies, the agreement between the UTD model and experiment remains consistently good. Figs. 13 and 14 show the results for Plate B at 11.2 GHz, and Figs. 15 and 16 show the results for 12.1 GHz.
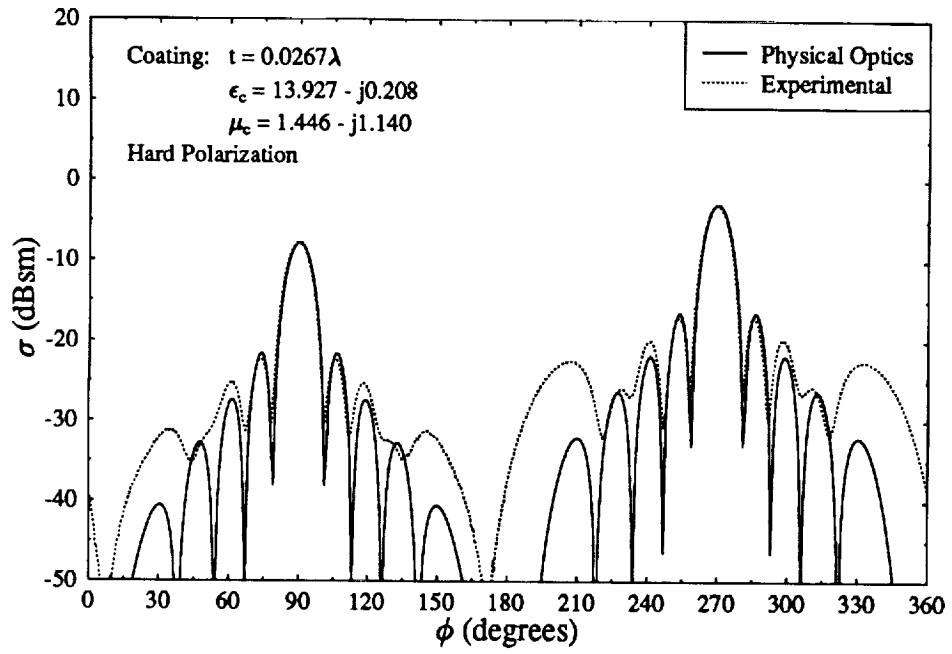
Figure 11: Monostatic RCS of Plate B ($w = L = 2.54\lambda$, $f = 9.5$ GHz).
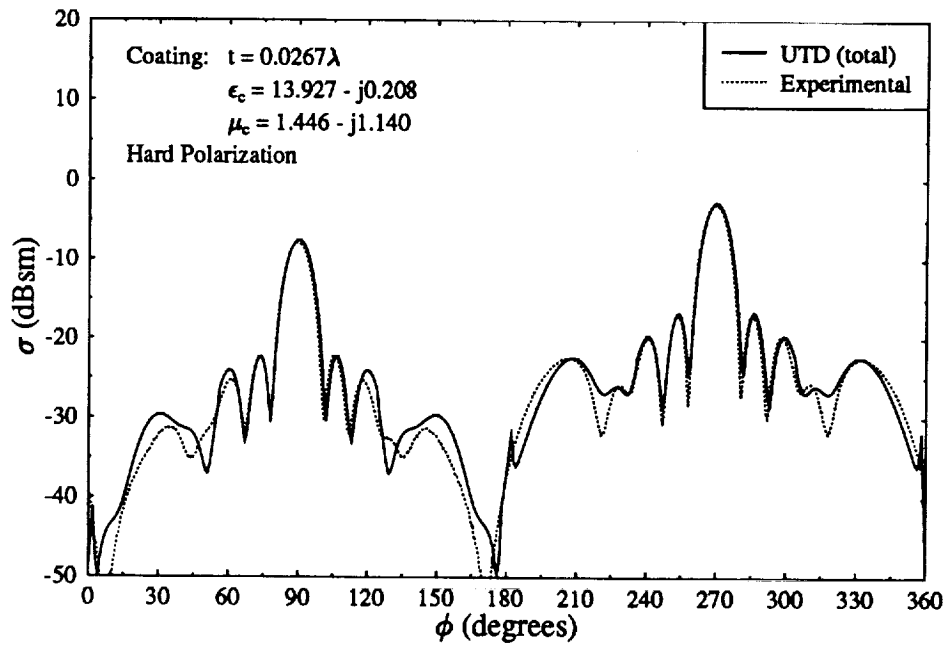

Figure 12: Monostatic RCS of Plate B ($w = L = 2.54\lambda$, $f = 9.5$ GHz).
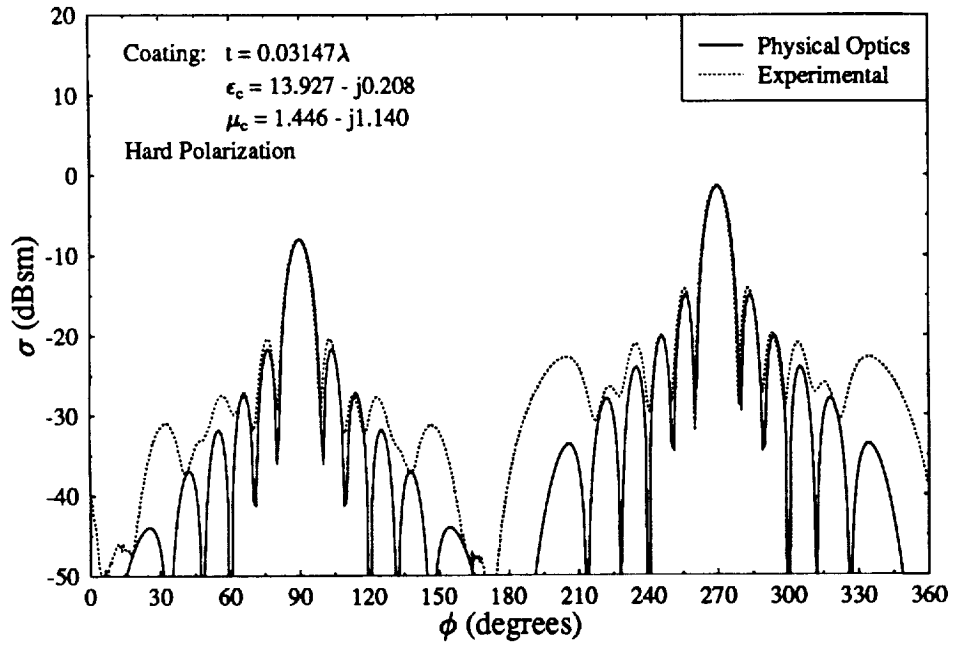
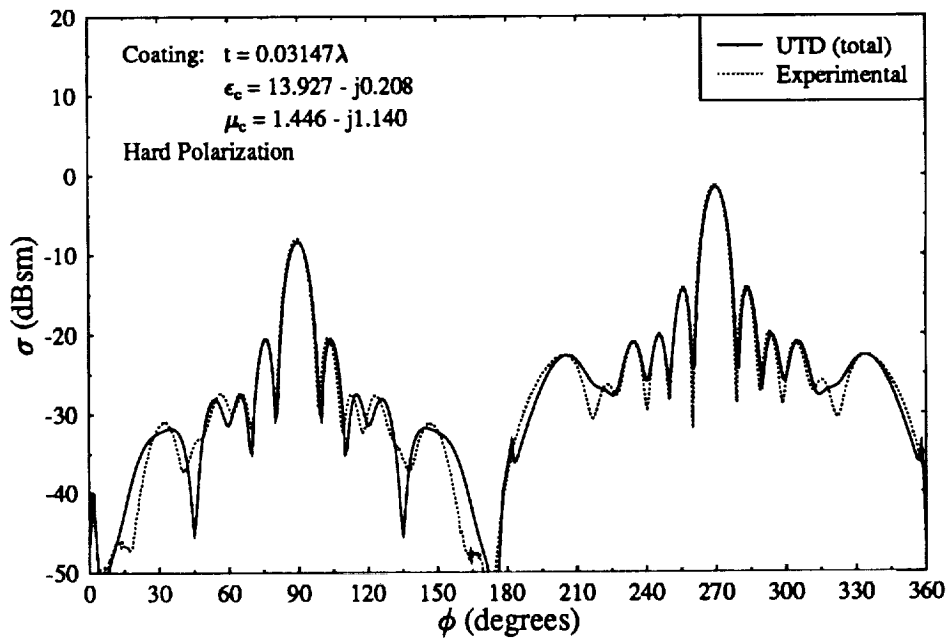Figure 13: Monostatic RCS of Plate B ($w = L = 3.0\lambda$, $f = 11.2$ GHz).

Figure 14: Monostatic RCS of Plate B ($w = L = 3.0\lambda$, $f = 10.0$ GHz).
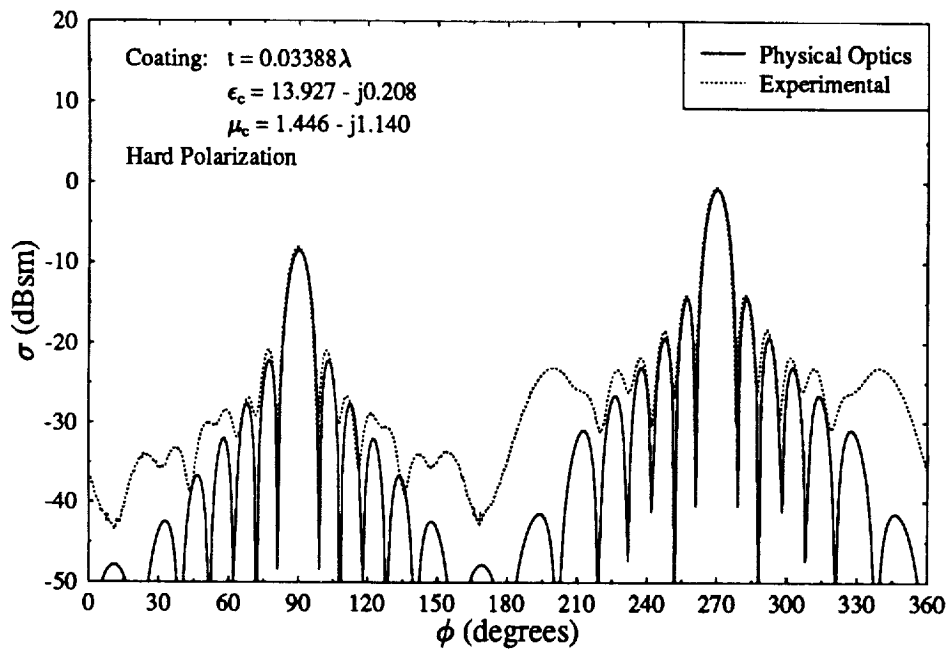
19

Figure 15: Monostatic RCS of Plate B ($w = L = 3.23\lambda$, $f = 12.1$ GHz).
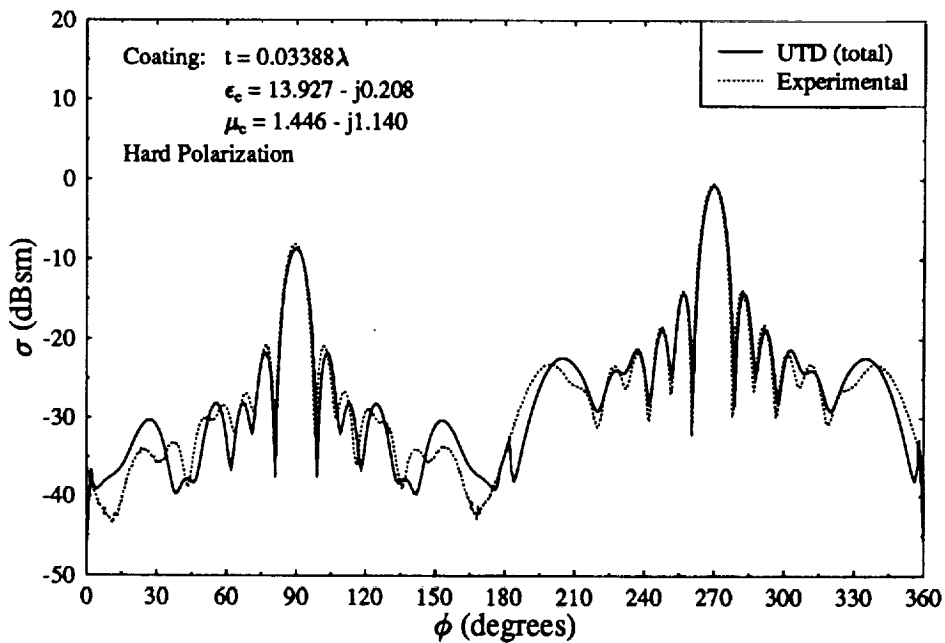

Figure 16: Monostatic RCS of Plate B ($w = L = 3.23\lambda$, $f = 12.1$ GHz).

C. FUTURE WORK

We have demonstrated a fairly accurate, yet computationally simple and fast, UTD model for coated plate scattering in the principal plane. Immediate future work will address modifications and refinements of this model. Particularly, the more accurate UTD diffraction coefficients formulated by Tiberio, *et al.* [13], will be used for modeling higher-order diffractions. This should result in better accuracy. Also, the use of the ESRM of Herman and Volakis [15] will be investigated to see if more accurate results can be obtained using this method.

The ultimate goal of this research is to be able to apply the UTD for coated wedges to general geometries. In order to realize this goal, the method must remain general. Other areas of possible future research include the use of the ESRM and of higher-order generalized impedance boundary conditions (GIBC's); however, the drawback of these techniques is that they are specific to a geometry and must often be reformulated for each target of interest. Also, although the area of GIBC's is promising, current research indicates that using GIBC's often results in non-unique solutions [21]. Despite these drawbacks, future research will look at the possibility of including the ESRM and GIBC's in a UTD model. Other future goals include extending the principal-plane plate model to nonprincipal planes by incorporating equivalent currents techniques. Also, the UTD for coated wedges will be applied to the dihedral corner reflector.

II. A PHYSICAL OPTICS/ EQUIVALENT CURRENTS MODEL FOR THE RCS OF TRIHEDRAL CORNER REFLECTORS

A. INTRODUCTION

In the last report we examined the radar cross section (RCS) of the square trihedral corner reflector in the interior region. Expressions for the reflected fields as well as expressions for the equivalent currents at the edges of the trihedral were explicitly given. In this report we examine the RCS of both the square and triangular corner reflectors. The formulation of the reflected fields for the interior region of the triangular trihedral is exactly the same as that of the square trihedral; however, the area over which the Physical Optics (PO) surface integral is evaluated is now different. The approach followed to determine this area of integration is explained thoroughly in this report. The equivalent currents at the exterior edges of either trihedral were derived based upon Michaeli's PTD equivalent edge currents. The PTD-EEC expressions for the triangular trihedral are also similar to those already used in the case of the square trihedral but now the orientation of the edges is different. Furthermore, in this report we include more results, for both the square and triangular trihedrals, which are compared with Finite-Difference Time-Domain (FDTD) data as well as with measurements performed in the ElectroMagnetic Anechoic Chamber (EMAC) at Arizona State University. The PO-MEC results compare very well with both the FDTD data and the measured data.

Analysis of a square trihedral corner reflector was performed by Baldauf et al. [22], using the CAD-based Shooting and Bouncing Ray (SBR) method. They examined both its monostatic and bistatic RCS for three different sizes (small, medium, and large). Their results were good for medium and large trihedrals but less accurate for smaller objects. The SBR method has the disadvantage that both

its accuracy and the CPU time required to run a particular case depend on the number of rays per wavelength launched from the incident direction toward the target. Increasing the density of the rays leads to more accurate results but at the expense of extending the CPU time. The accuracy of the method is proportional to the number of rays because the fields at the aperture of the output ray tube are approximated to those that correspond to the ray passing through the center of the aperture. As the number of rays per wavelength increases, the area of the aperture eventually becomes very small and the approximation becomes more appropriate. In other words, the smaller the aperture of the output ray tube is, the more accurate the SBR results are; however, the CPU time increases because of the use of a denser grid. Also, the CPU time increases with increasing radar target size. This is not a very attractive feature for a high frequency approach such as the SBR method.

In the present analysis, PO and Michaeli's equivalent edge currents (EEC) method (usually referred as PTD-EEC) are applied on both the square and tri-angular trihedral corner reflectors to evaluate the backscatter RCS in the interior region. PO is used for the calculation of single, double, and triple reflections from the trihedral plates, whereas PTD-EEC is used for the calculation of the first-order diffractions from the exterior edges. The PO surface current density is integrated over the illuminated area of the particular plate. For single reflections the surface integration is evaluated over the entire plate because it is completely illuminated. The integration is carried out in closed form since the integrand is a simple exponential function with linearly varying phase over the entire surface of the plate. For double and triple reflections, however, the surface of integration is not the entire area of the second and third plates, respectively, but rather only the illuminated parts of these plates. The shape of the illuminated area is usually an arbitrary polygon whose shape changes according to the incident and observation angles. The difficulty in this case is to determine the shape of the illuminated area at any incident angle and to efficiently integrate the surface current density over

that area. Another problem with the evaluation of the double and triple reflected fields is the fact that the surface current density on the second and third plates of the trihedral should be calculated in the "near field" of the first and second reflections, respectively. In our analysis, however, the GO approximation is used for the calculation of the initial reflected fields and the PO is subsequently applied only for the last reflection. In other words, it is assumed that the planar nature of the incident wave is maintained after the first and second reflections, which simplifies the expressions for the scattered fields considerably.

For the evaluation of the diffracted fields, Michaeli's PTD-EEC expressions are utilized to calculate the first-order diffractions from the exterior edges of the trihedral. Diffractions from interior edges are usually much lower than diffractions from exterior edges and, therefore, were excluded. PTD-EEC expressions are based on the fringe component of the equivalent edge current for the wedge. These were deduced from the exact solution of the canonical wedge problem. It is also important to note that PTD-EEC expressions do not contain the PO component of equivalent currents; therefore, the diffracted fields using PTD-EEC should improve the reflected fields calculated using PO. In the case of the trihedral, however, the reflected fields in the interior region are significantly higher than the diffracted fields. Consequently, the effect of the diffractions is not always obvious.

B.   ANALYSIS

The backscatter cross section of the square and triangular trihedral corner reflectors, depicted in Figs. 17(a) and 17(b), is evaluated by considering single, double, and triple reflections as well as first-order diffractions. Expressions for the reflected fields were given explicitly in the previous report; therefore, they are not repeated here. It is important, however, that the approach used to determine the shape of the illuminated area on the plate of last reflection be explained in detail. This is the area on which the PO integration is evaluated. For single reflections the illuminated area is the entire surface of the particular plate. For double and
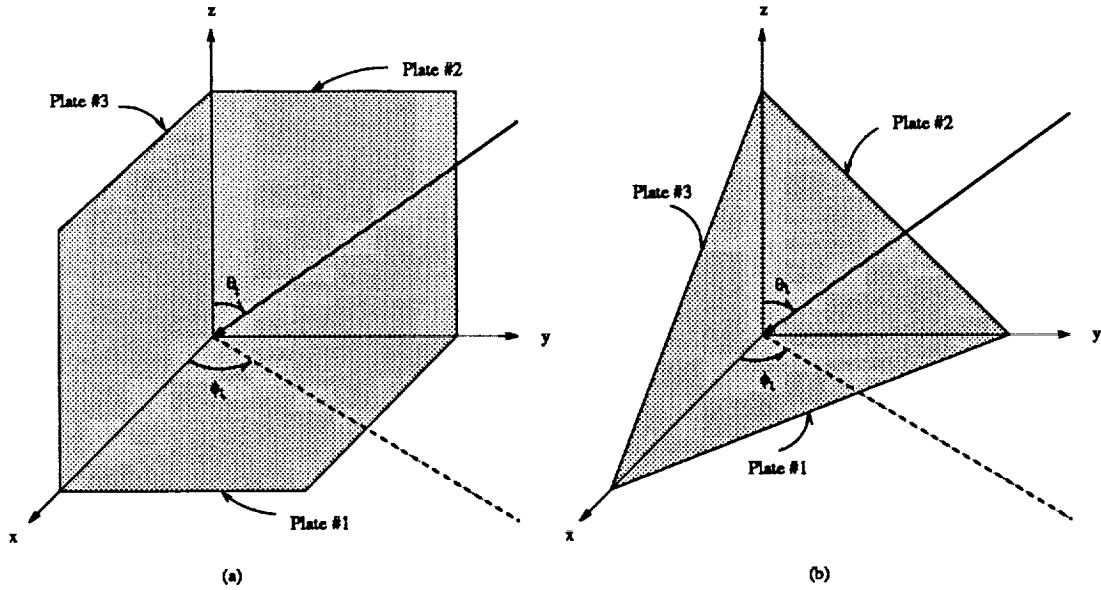
24

Figure 17: Geometry of the square and triangular trihedrals.

triple reflections the illuminated area looks like an arbitrary polygon whose shape depends on the incident angles.

1. The Shape of the Illuminated Area for Double and Triple Reflections

Evaluation of the doubly and triply reflected fields requires integration over the illuminated part of the plate on which the last reflection occurs. The illuminated area on that plate has the shape of a polygon whose corner coordinates vary according to the direction of incidence. Our objective in this section is to explain how the corner coordinates of the illuminated area can be determined, as well as to illustrate an efficient way to evaluate the PO surface integral over this area.

Double and triple reflections occurring in the interior of a trihedral corner reflector create shadow regions on the second and third plate, respectively. Fig. 18(a) illustrates the shaded area created on plate #3 for the case of the double reflection term R_{23}. As is shown, the incident plane wave, which illuminates completely all three trihedral plates, is first reflected from plate #2 and then propagates toward plate #3. However, the reflected fields from plate #2 do not completely illuminate plate #3. To determine the shape of the illuminated and/or shadow region

25

on plate #3, it is first necessary to obtain the direction of the rays after the first reflection occurs. Their direction, according to image theory, is the mirror image of the incident direction over plate #2. Knowing the direction of the reflected rays from plate #2, one can trace the path of the rays that pass through the exterior edges of plate #2, as shown in Fig. 18(a), to the point where they reach the surface of plate #3. We do not trace the path of the rays that do not strike plate #3. The line connecting the points where these ray-paths intersect with plate #3, referring to Fig. 18(a), defines the boundary that separates the illuminated from the shadow region. The illuminated area should always include the origin of the coordinate system. Note that the shape of the illuminated area varies with the incident angle. To illustrate this, two cases with different directions of incidence are examined. Fig. 18(a) depicts the shadow region on plate #3 for incident angles θ_i greater than 45° and ϕ_i also greater than 45°. As θ_i becomes smaller than 45°, the shape of the illuminated area looks like a triangle, as shown in Fig. 18(b).

For triple reflections, estimating the shaded part on the third plate after two consecutive reflections on the other two trihedral plates is much more complicated than in the case of double reflections. The approach, however, remains the same as before — the double reflected rays passing through the periphery of the illuminated area on the second plate, see Fig. 18(c), are traced to the third plate. These rays intersect the surface of the third plate at certain points, which actually mark the boundary of the illuminated area (or shaded area). The shaded area on the third plate for the case of the triple reflection term $R123$ is ilustrated in Fig. 18(c).

As demonstrated above, the illuminated area on a particular plate due to either double or triple reflection is a polygon whose shape depends on the direction of wave incidence. To calculate the reflected fields, the PO surface integral should be evaluated on this polygon. An efficient way to evaluate this integral is to subdivide the corresponding polygon into rectangles and right triangles. The PO surface integral can then be easily evaluated over the areas of both these two shapes in closed form.
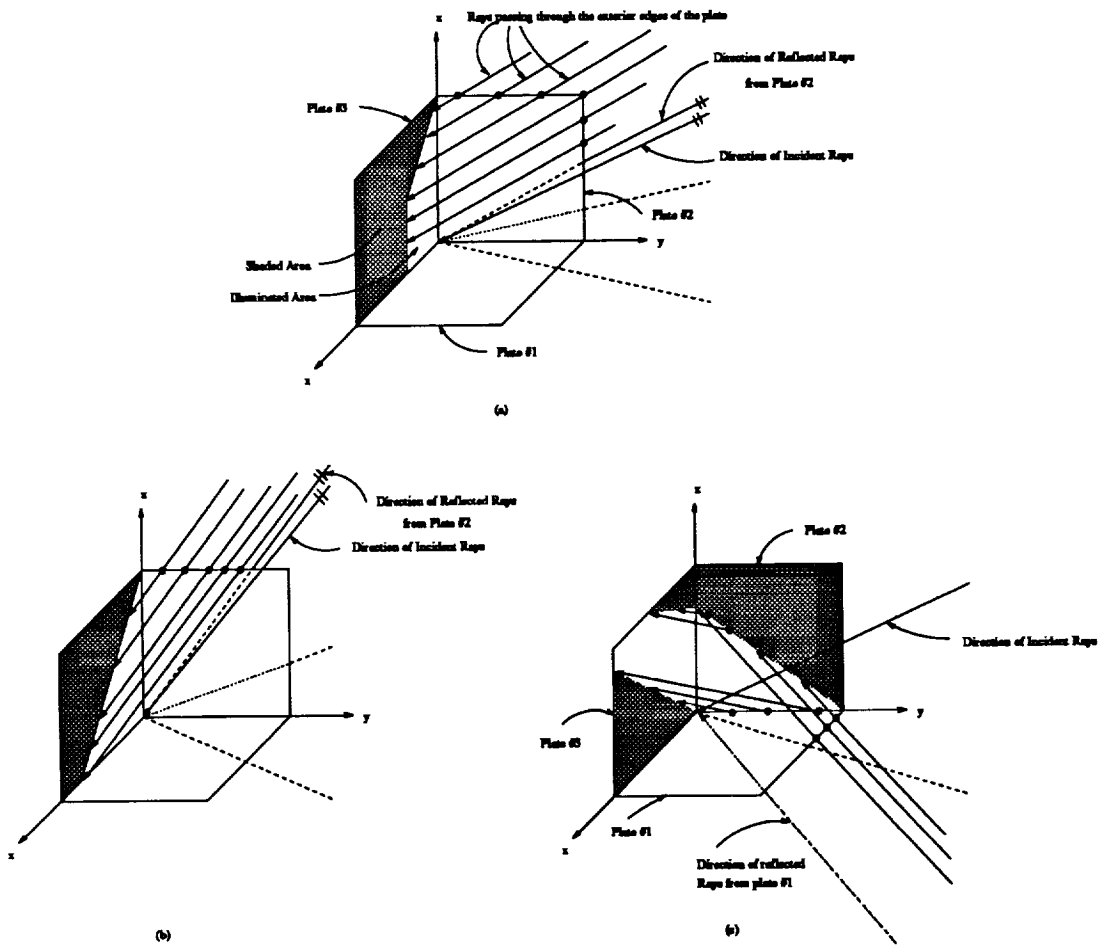
26

Figure 18: Shading due to multiple reflections by the interior of the trihedral.

2. Evaluation of Diffracted Fields Using PTD-EEC

PTD-EEC expressions, derived by Michaeli [23, 24], are utilized to find the far-field diffracted fields from the exterior edges of both the square and the triangular trihedral corner reflectors. PTD-EEC expressions are based on the fringe currents that exist at the edges. Unlike GTD-EEC, PTD-EEC does not include the PO surface current density. Therefore, adding the diffracted fields (based on the PTD-EEC formulations) to the reflected fields (based on the PO surface current density) results in closer agreement with the experimental data. The corresponding expressions for the fringe currents, I^f and M^f, can be found in Michaeli's papers on equivalent currents [23, 24]. Here, the analysis is restricted to how the electric and magnetic fringe currents are used to derive expressions for the far-field diffracted fields. The procedure is similar to the one used for the reflected fields in the previous section. First, the vector potentials are estimated using

$$\mathbf{A} = \frac{\mu}{4\pi} \int_C \mathbf{I}^f \frac{e^{-jkR}}{R} dl \simeq \frac{\mu}{4\pi} \frac{e^{-jkr}}{r} \int_C \mathbf{I}^f e^{jk L_s} dl \qquad (6)$$

$$\mathbf{F} = \frac{\epsilon}{4\pi} \int_C \mathbf{M}^f \frac{e^{-jkR}}{R} dl \simeq \frac{\epsilon}{4\pi} \frac{e^{-jkr}}{r} \int_C \mathbf{M}^f e^{jk L_s} dl \qquad (7)$$

where L_s was defined in the previous report. The integral is evaluated along the length of the trihedral edge from which the diffracted fields are to be calculated. As in the case of reflected fields from a trihedral plate, this integral can be evaluated in closed form because the integrand is a simple exponential function with linearly varying phase along the edge. After evaluating the electric and magnetic vector potentials, the far-field spherical components of the scattered field can be written as [25]

$$E_r \simeq 0 \qquad (8)$$

$$E_\theta \simeq -j\omega(A_\theta + \eta F_\phi) \qquad (9)$$

$$E_\phi \simeq -j\omega(A_\phi - \eta F_\theta) \qquad (10)$$

28

C. RESULTS

Results from the combined PO-MEC model are compared with experimental data, as well as with data obtained using the FDTD method. The experiments were performed using both a square and a triangular corner reflector whose geometries are shown in Figs. 17(a) and 17(b).

The main advantage of the PO-MEC approach, over other techniques, is that it calculates each scattering component separately and then combines them for the calculation of the total RCS. Each component (single, double, trible reflections and first-order diffractions), therefore, can be plotted separately in order to examine its contribution to the total RCS. Then, the shape of the particular target can be slightly modified to reduce the RCS of the component that contributes the most to the total backscattered fields. Fig. 19 illustrates the major individual backscattering components of a 15λ square trihedral for $\theta_i = \theta_s = 50°$ and $\phi_i = \phi_s$ varying from 0° to 90°. These RCS plots represent single reflections (R_1, R_2, and R_3), double reflections (R_{12}, R_{13}, R_{21}, R_{23}, R_{31}, and R_{32}), triple reflections (R_{123}, R_{132}, R_{213}, R_{231}, R_{312}, and R_{321}), and first-order diffractions from the exterior edges of the square trihedral plates. Diffractions from the three interior edges of the trihedral were not considered, which explains why the RCS pattern for the first-order diffractions is not completely symmetric about 45°. Fig. 19 also illustrates the total RCS pattern of the square trihedral. Examining these five figures, it can be seen that the major contribution to the RCS is provided by the triply reflected fields. The reason is that all three trihedral plates are mutually perpendicular; therefore, the direction of propagation of the triply reflected fields is parallel to that of the incident plane wave. Changing the angle between the plates will certainly reduce the overall RCS.

To adequately validate the approach followed in this paper, different sizes of both trihedral corner reflectors were considered. All graphs in this section correspond to E_θ polarization.
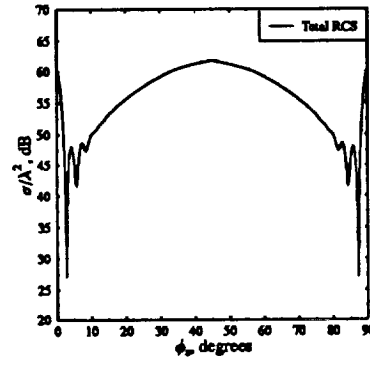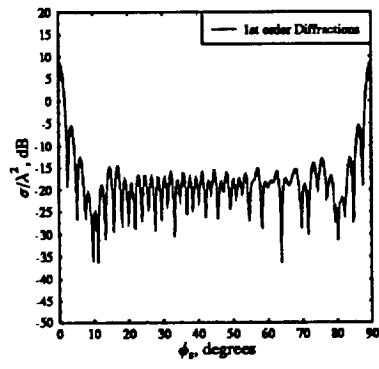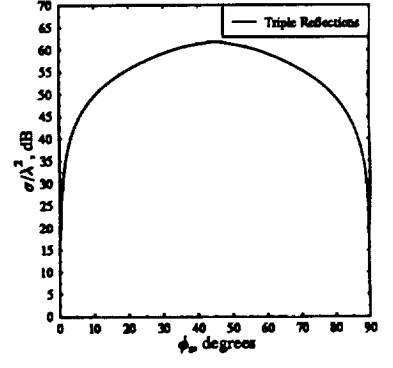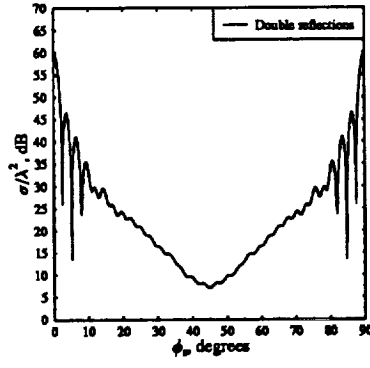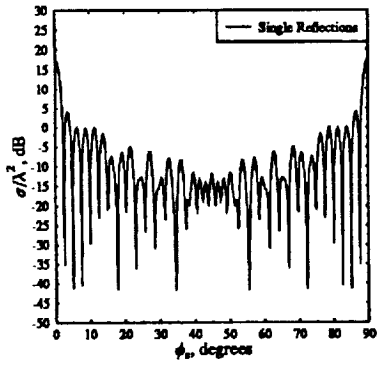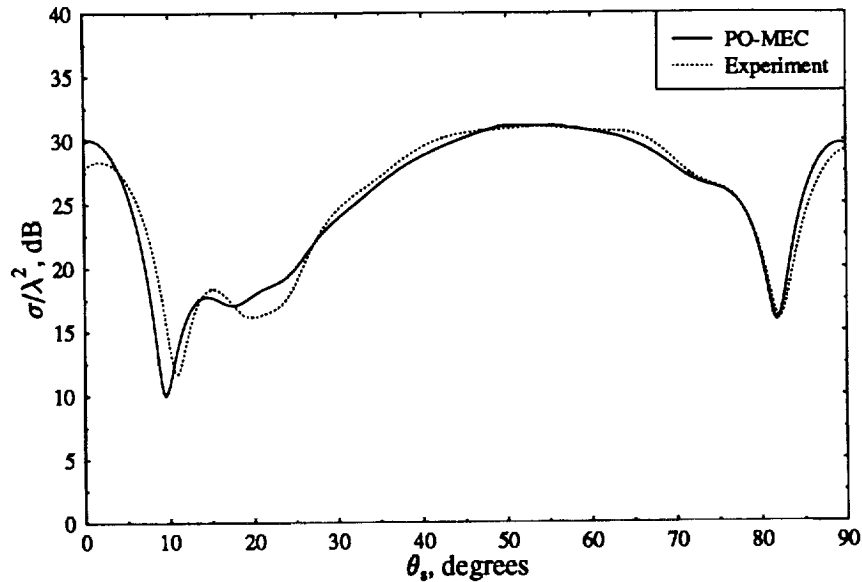
Figure 19: Breakdown of scattering into individual components.

Figure 20: Monostatic RCS of a 3λ square trihedral at $\phi_i = \phi_s = 60°$.

1. Small Trihedral Corner Reflectors

A 3λ square trihedral and a 5λ triangular trihedral are considered relatively small radar targets for high frequency analysis. The classification of small, medium and large trihedrals is based on the total area covered by the trihedral plates. Fig. 20 shows the monostatic RCS of a 3λ square trihedral at $\phi_i = \phi_s = 60°$ as $\theta_i = \theta_s$ varies from $0°$ to $90°$. The agreement between the predicted and the experimental results is good even if the object is relatively small for high frequency analysis. Fig. 21 shows the monostatic RCS of a 5λ triangular trihedral at $\phi_i = \phi_s = 35°$ as $\theta_i = \theta_s$ varies from $0°$ to $90°$. A very good agreement between the theoretical and the experimental results is observed.
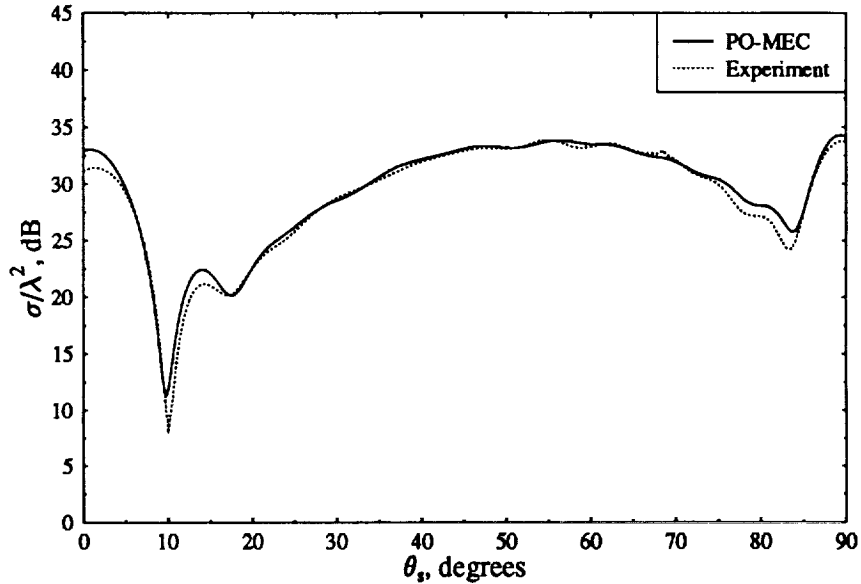
31

Figure 21: Monostatic RCS of a 5λ triangular trihedral at $\phi_i = \phi_s = 35°$.

2. Medium Trihedral Corner Reflectors

A 5λ square trihedral and a 7λ triangular trihedral are considered medium sized radar targets. Fig. 22 shows the monostatic RCS of the 5λ square trihedral on a conical path where $\theta_i = \theta_s = 66°$ and $\phi_i = \phi_s$ varies from $0°$ to $90°$. Our predictions are compared with both FDTD and measured data. The agreement is very good.

In addition to conical paths, our formulation is capable of calculating the RCS of either the square or triangular trihedral by moving the source and/or observation point along a great circle. The great circle has its center at the origin of the coordinate system and makes an angle $\theta = \theta_g$ with the z-axis at $\phi = 45°$. This is the same as if the trihedral is tilted forward so its z-directed edge makes an angle $90 - \theta_g$ degrees with the z-axis as ϕ_s changes from $0°$ to $90°$. Fig. 23 shows the monostatic RCS of a 7λ triangular trihedral as ϕ_s varies on a great circle at $\theta_g = 80°$. The agreement between theoretical and experimental data is very good. Also, observe that the RCS patterns of Figs. 22 and 23 are symmetric about
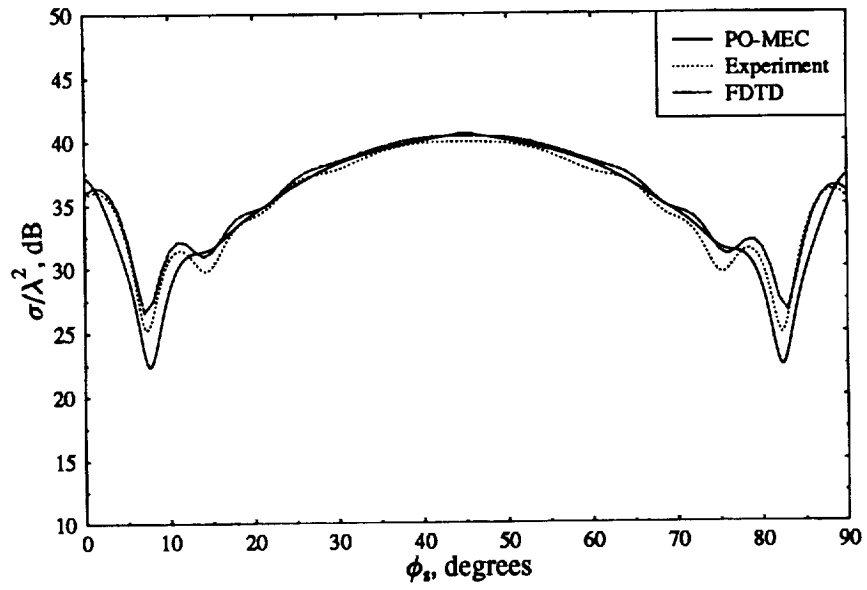
32

Figure 22: Monostatic RCS of a 5λ square trihedral at $\theta_i = \theta_s = 66°$.
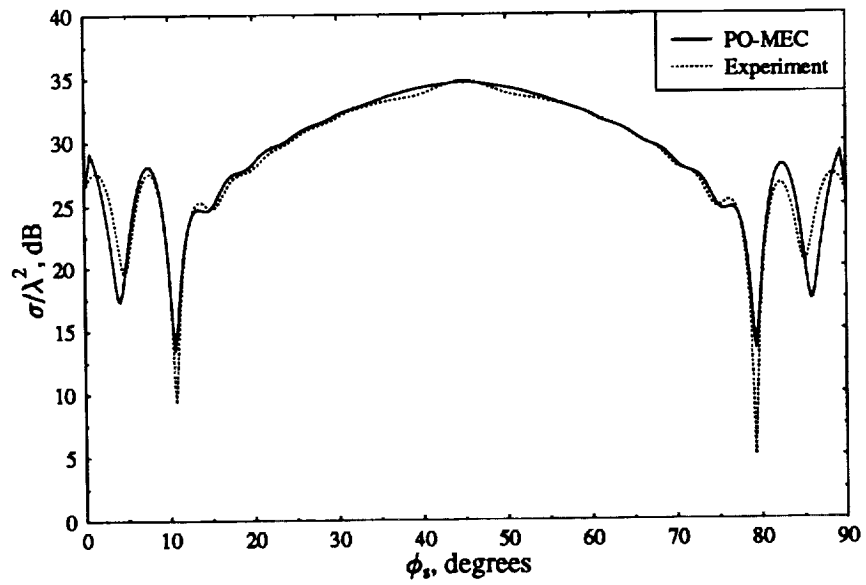

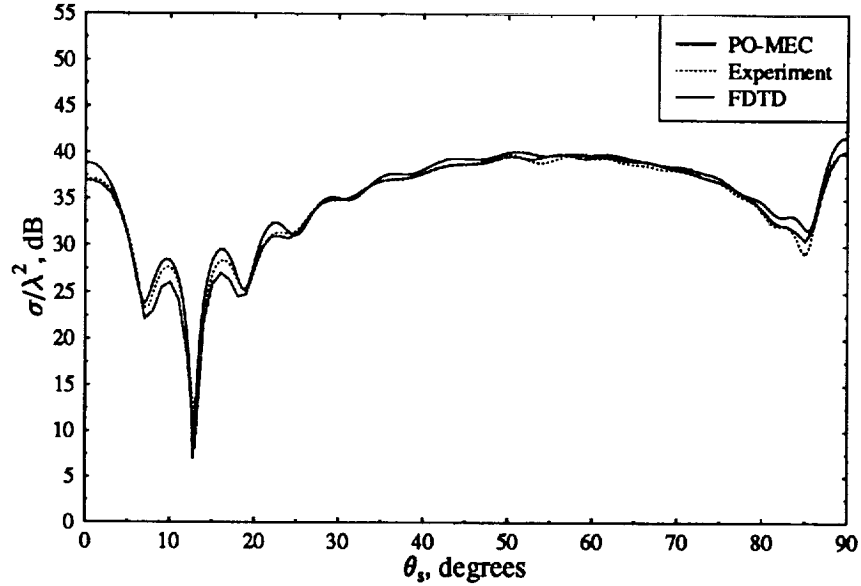Figure 23: Monostatic RCS of a 7λ triangular trihedral on a great circle at $\theta_g = 80°$.

Figure 24: Monostatic RCS of a 7λ triangular trihedral at $\phi_i = \phi_s = 45°$.

$\phi = 45°$. This is always the case since the trihedral exhibits symmetry when the observation point moves on an azimuthal plane. Fig. 24 illustrates the monostatic RCS of a 7λ triangular trihedral at $\phi_i = \phi_s = 45°$ as $\theta_i = \theta_s$ varies from $0°$ to $90°$. Our predictions match very well with both the FDTD and the experiment.

3. Large Trihedral Corner Reflectors

A 7λ square trihedral and a 10λ triangular trihedral are considered relatively large radar targets. Fig. 25 shows the monostatic RCS of a 7λ square trihedral on a conical path as $\theta_i = \theta_s = 70°$ and $\phi_i = \phi_s$ varies from $0°$ to $90°$. The agreement of the PO-MEC with the experiment is very good. Fig. 26 shows the monostatic RCS of a 7λ square trihedral at $\phi_i = \phi_s = 50°$ as $\theta_i = \theta_s$ varies from $0°$ to $90°$. Our predictions agree very well with the FDTD data. Fig. 27 shows the monostatic RCS of a 10λ triangular trihedral as ϕ_s varies on a great circle at $\theta_g = 80°$. The agreement of the PO-MEC with the experiment is very good except near $\phi_s = 7°$;
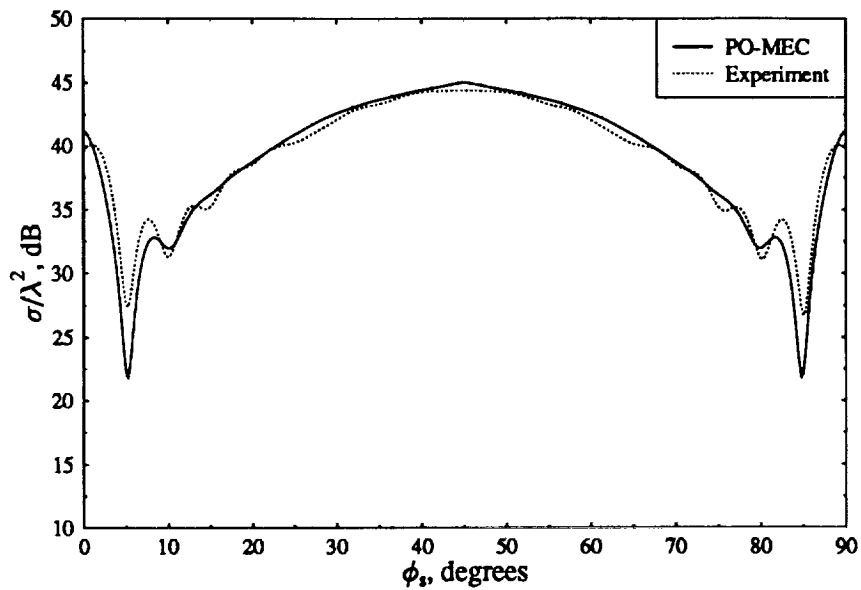
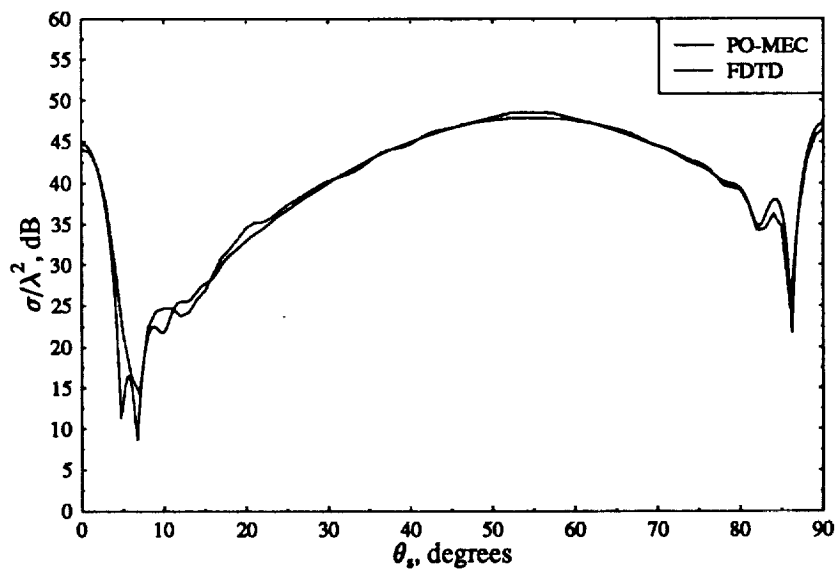Figure 25: Monostatic RCS of a 7λ square trihedral at $\theta_i = \theta_s = 80°$.

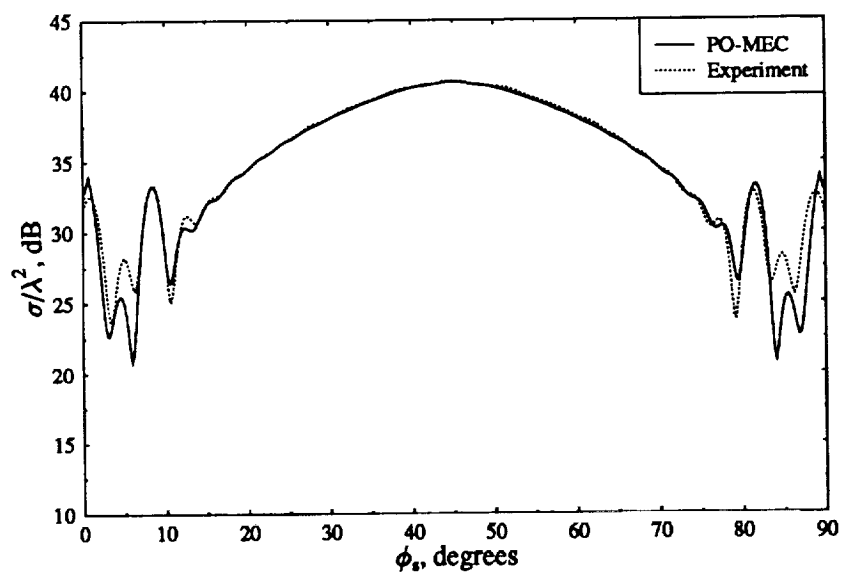Figure 26: Monostatic RCS of a 7λ square trihedral at $\phi_i = \phi_s = 50°$.

Figure 27: Monostatic RCS of a 10λ triangular trihedral on a great circle at $\theta_g = 80°$.
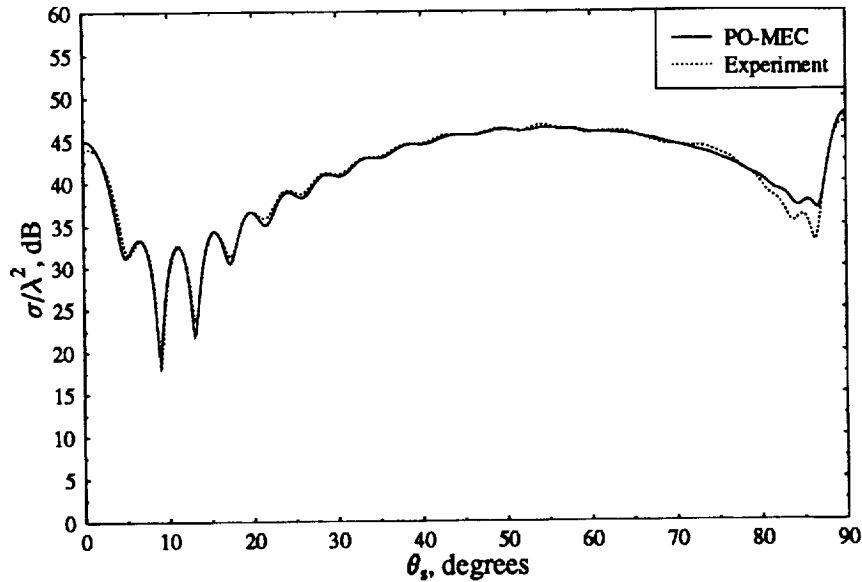
Figure 28: Monostatic RCS of a 10λ square trihedral at $\phi_i = \phi_s = 45°$.

however, it was observed that near this specific observation angle the RCS pattern is very sensitive to slight changes in θ_g. Also, it can be seen from Fig. 27 that the experimental data is not quite symmetric about $\phi_s = 45°$. Finally, Fig. 28 shows the monostatic RCS of a 10λ triangular trihedral at $\phi_i = \phi_s = 45°$ as $\theta_i = \theta_s$ varies from $0°$ to $90°$. Our predictions are in nearly excellent agreement with the experimental data.

The FORTRAN code written for the evaluation of the RCS of either the square or the triangular trihedral corner reflector provides very good results for any angle of incidence and/or observation. The agreement with experimental data is within 2 dB of accuracy. Fig. 29 and Fig. 30 show three-dimensional RCS patterns of a 5λ square trihedral and a 7λ triangular trihedral, respectively. The execution time required by a SUN SPARC station IPX computer to calculate the data to create either one of these three-dimensional plots is 77.4 seconds, which is much less than the execution time required by other theoretical techniques to
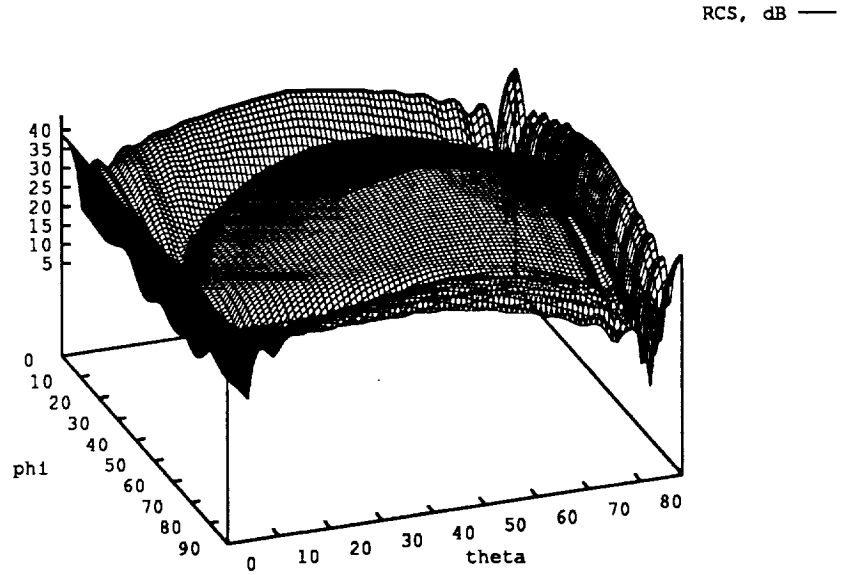
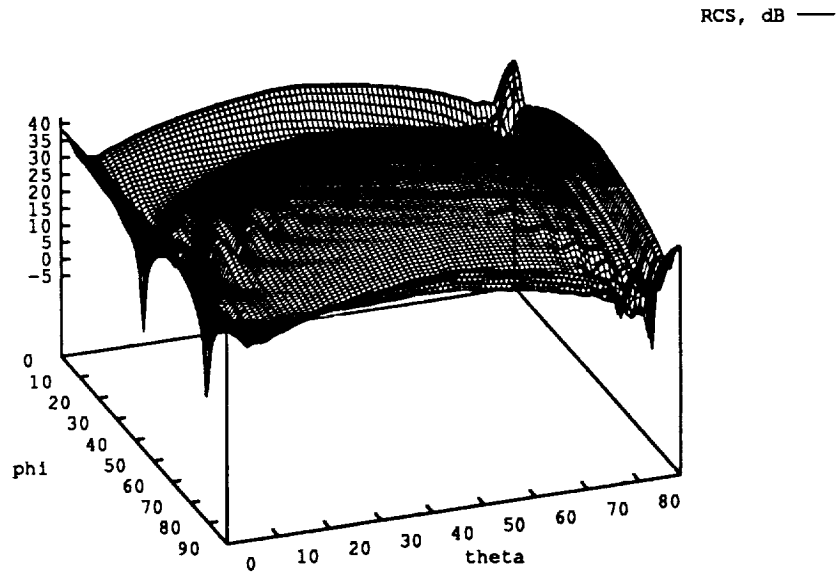Figure 29: Three-dimensional monostatic RCS of a 5λ square trihedral.

Figure 30: Three-dimensional monostatic RCS of a 7λ triangular trihedral.

38

perform the same task.

D. CONCLUSIONS

The hybridization of PO and MEC is a very good approach for the evaluation of the monostatic RCS of complex structures such as the square and triangular corner reflectors. It provides results that compare very well with experimental, as well as with FDTD data. The method is also very efficient in terms of computational requirements such as memory space and CPU time. For example, the FORTRAN code, which was used to obtain the results presented in this report, can compile and run on a variety of computer systems including a PC. It also runs very quickly. Specifically, it takes only 0.0095 seconds on a SUN SPARC station IPX computer to evaluate the RCS of either trihedral corner reflector at a single point. This CPU time is constant, regardless of the trihedral size.

E. FUTURE WORK

In this semiannual report we examined the monostatic RCS of both square and triangular trihedral corner reflectors in the interior region. In the future, we are planning to obtain the RCS of both these trihedrals in the exterior region as well. This will complicate the approach used to determine the illuminated area on the plate of last reflection.

References

[1] C. A. Balanis and L. A. Polka, "Nonprincipal plane scattering of flat plates," Semiannual Report, Grant No. NAG-1-562, National Aeronautics and Space Administration, Langley Research Center, Hampton, VA, Jan. 31, 1989.

[2] C. A. Balanis and L. A. Polka, "Nonprincipal plane scattering of flat plates — second-order and corner diffraction," Semiannual Report, Grant No. NAG-1-562, National Aeronautics and Space Administration, Langley Research Center, Hampton, VA, Jul. 31, 1989.

[3] C. A. Balanis, L. A. Polka, and K. Liu, "Nonprincipal plane scattering from rectangular plates and pattern control of horn antennas," Semiannual Report,

Grant No. NAG-1-562, National Aeronautics and Space Administration, Langley Research Center, Hampton, VA, Jan. 31, 1990.

[4] C. A. Balanis, L. A. Polka, and K. Liu, "Scattering from coated structures and antenna pattern control using impedance surfaces," Semiannual Report, Grant No. NAG-1-562, National Aeronautics and Space Administration, Langley Research Center, Hampton, VA, Jul. 31, 1990.

[5] C. A. Balanis and L. A. Polka, "High-frequency techniques for RCS prediction of plate geometries," Semiannual Report, Grant No. NAG-1-562, National Aeronautics and Space Administration, Langley Research Center, Hampton, VA, Jan. 31, 1991.

[6] C. A. Balanis and L. A. Polka, "High-frequency techniques for RCS prediction of plate geometries," Semiannual Report, Grant No. NAG-1-562, National Aeronautics and Space Administration, Langley Research Center, Hampton, VA, Jul. 31, 1991.

[7] C. A. Balanis and L. A. Polka, "High-frequency techniques for RCS prediction of plate geometries," Semiannual Report, Grant No. NAG-1-562, National Aeronautics and Space Administration, Langley Research Center, Hampton, VA, Jan. 31, 1992.

[8] C. A. Balanis and L. A. Polka, "High-frequency techniques for RCS prediction of plate geometries," Semiannual Report, Grant No. NAG-1-562, National Aeronautics and Space Administration, Langley Research Center, Hampton, VA, Jul. 31, 1992.

[9] C. A. Balanis, L. A. Polka, and A. C. Polycarpou, "High-frequency techniques for RCS prediction of plate geometries and a physical optics/equivalent currents model for the RCS of trihedral corner reflectors," Semiannual Report, Grant No. NAG-1-562, National Aeronautics and Space Administration, Langley Research Center, Hampton, VA, Jan. 31, 1993.

[10] C. M. Knop and G. I. Cohn, "On the radar cross section of a coated plate," *IEEE Trans. Antennas Propagat.*, vol. AP-11, pp. 719–721, Nov. 1963.

[11] A. K. Bhattacharyya and S. K. Tandon, "Radar cross section of a finite planar structure coated with a lossy dielectric," *IEEE Trans. Antennas Propagat.*, vol. AP-32, pp. 1003–1007, Sept. 1984.

[12] E. H. Newman and M. R. Schrote, "An open surface integral formulation for electromagnetic scattering by material plates," *IEEE Trans. Antennas Propagat.*, vol. AP-32, pp. 672–678, Jul. 1984.

[13] R. Tiberio, G. Pelosi, and G. Manara, "A uniform GTD formulation for the diffraction by a wedge with impedance faces," *IEEE Trans. Antennas Propagat.*, vol. AP-33, pp. 867 – 873, Aug. 1985.

[14] T. Griesser and C. A. Balanis, "Reflections, diffractions, and surface waves for an interior impedance wedge of arbitrary angle," *IEEE Trans. Antennas Propagat.*, vol. AP-37, pp. 927 – 935, Jul. 1989.

[15] M. I. Herman and J. L. Volakis, "High frequency scattering from polygonal impedance cylinders and strips," *IEEE Trans. Antennas Propagat.*, vol. AP-36, pp. 679–689, May 1988.

[16] J. L. Volakis and T. B. A. Senior, "Application of a class of generalized boundary conditions to scattering by a metal-backed dielectric half-plane," *Proc. IEEE*, vol. 77, pp. 796–805, May 1989.

[17] R. G. Rojas and L. M. Chou, "Diffraction by a partially coated perfect electric conducting half plane," *Radio Sci.*, vol. 25, pp. 175–188, Mar. - Apr. 1990.

[18] J.-M. L. Bernard, "Diffraction by a metallic wedge covered with a dielectric material," *Wave Motion*, vol. 9, pp. 543–561, Nov. 1987.

[19] R. A. Ross, "Radar cross section of rectangular flat plates as function of aspect angle," *IEEE Trans. Antennas Propagat.*, vol. AP-14, pp. 329 – 335, May 1966.

[20] G. D. Maliuzhinets, "Excitation, reflection and emission of surface waves from a wedge with given face impedances," *Sov. Phys. Doklady*, vol. 3, pp. 752 – 755, Jul./Aug. 1958.

[21] T. B. A. Senior, *Derivation and Application of Approximate Boundary Conditions*, pp. 477–483. *Directions in Electromagnetic Wave Modeling (H. L. Bertoni and L. B. Felsen, eds.)*, New York: McGraw-Hill, 1969.

[22] J. Baldauf, S. W. Lee, L. Lin, S. K. Jeng, S. M. Scarborough, and C. L. Yu, "High frequency scattering from trihedral corner reflectors and other benchmark targets: SBR versus experiment," *IEEE Trans. Antennas Propagat.*, vol. AP-39, pp. 1345–1351, Sep. 1991.

[23] A. Michaeli, "Equivalent edge currents of arbitrary aspects of observation," *IEEE Trans. Antennas Propagat.*, vol. AP-32, pp. 252–258, Mar. 1984.

[24] A. Michaeli, "Elimination of infinities in equivalent edge currents, part I: Fringe currents," *IEEE Trans. Antennas Propagat.*, vol. AP-34, pp. 912–918, Jul. 1986.

[25] C. A. Balanis, *Advanced Engineering Electromagnetics*. New York: John Wiley and Sons, 1989.